Theoretical analysis of full-ring multi-pinhole brain SPECT

2009 Phys. Med. Biol. 54 6593

(http://iopscience.iop.org/0031-9155/54/21/010)

Phys. Med. Biol. **54** (2009) 6593–6610 doi:10.1088/0031-9155/54/21/010

Theoretical analysis of full-ring multi-pinhole brain SPECT

M C Goorden[1,2], M C M Rentmeester[1] and F J Beekman[1,2,3]

[1] Image Sciences Institute, University Medical Center Utrecht, STR 5.203, Universiteitsweg 100, 3584 CG Utrecht, The Netherlands
[2] Delft University of Technology, Section Radiation, Detection and Medical Imaging, Mekelweg 15, 2629 JB Delft, The Netherlands
[3] Molecular Imaging Laboratories, Heidelberglaan 100, 3584 CX Utrecht, The Netherlands

E-mail: m.c.goorden@tudelft.nl

Received 3 June 2009, in final form 21 September 2009
Published 14 October 2009
Online at stacks.iop.org/PMB/54/6593

Abstract

Presently used clinical brain SPECT suffers from limited spatio-temporal resolution. Here we investigate the feasibility of high-resolution and high-sensitivity full-ring multi-pinhole brain SPECT (MP-SPECT). Using an analytical model we optimized pinhole-detector geometries of MP-SPECT for different detector intrinsic resolutions R_i. System resolution and sensitivity of optimized MP-SPECT were compared to conventional clinical SPECT. The comparison of the system resolution of different systems was done at matched sensitivity, which was achieved by tuning pinhole diameters. Similarly, sensitivities were compared at matched system resolution. For MP-SPECT that uses detectors with intrinsic resolutions of 4 mm $> R_i \geqslant 0.5$ mm a sensitivity can be achieved that is 6.0 times higher than the sensitivity of conventional dual-head SPECT systems with parallel-hole collimators (DualPar), while system resolution can be improved by a factor of 2.4. To achieve these improvements a large detector-to-collimator distance is needed. In contrast, for detectors with intrinsic resolutions < 0.2 mm, it is beneficial to place the detectors close to the pinholes, resulting in a high number of de-magnified projections. For a detector intrinsic resolution of 0.05 mm, a 14.5-fold improvement in sensitivity and a 3.8-fold improvement in system resolution compared to DualPar is predicted. Furthermore, we found that for optimized MP-SPECT the sensitivity scales proportionally to system resolution squared, with the proportionality constant depending on R_i. From our sensitivity-system resolution trade-off equations we deduced that MP-SPECT with an ideal detector ($R_i \rightarrow 0$) can have a system resolution that is 2.0 times better than optimized MP-SPECT with a conventional detector ($R_i \simeq 3$ mm). The high performance of optimized MP-SPECT may open up completely new molecular imaging applications.

1. Introduction

Single-photon emission computed tomography (SPECT) is a well-established modality for imaging a broad variety of functional and molecular aspects of the human brain. Brain SPECT encompasses a wide variety of possible imaging studies, with typical radiopharmaceuticals such as ^{99m}Tc-ECD, ^{99m}Tc-HMPAO, ^{123}I-FP-CIT, ^{123}I-IBZM and ^{123}I-ADAM. ^{99m}Tc-ECD and ^{99m}Tc-HMPAO are employed to image brain perfusion, currently the most widely used application of brain SPECT. It permits the assessment of the cerebral metabolism, which is used in the evaluation of, for example, dementias, epilepsy, cerebrovascular disease and trauma. Other radioligands can assist in imaging various aspects of the neurotransmitter systems involved in brain function which can be useful in the study and diagnosis of depression, ADHD and Parkinson's disease. These include ^{123}I-FP-CIT and ^{123}I-IBZM for assessing presynaptic and postsynaptic dopaminergic function, respectively. ^{123}I-ADAM is a recently developed tracer used to image serotonine transporters (Verhoeff 2004). In addition, specific tracers are being developed for imaging processes related to Alzheimer's disease (Nordberg 2004, Kung *et al* 2004, Borroni *et al* 2006, McKeith *et al* 2007, Newberg *et al* 2007).

At present, SPECT devices employed for brain imaging are predominantly general-purpose SPECT devices equipped with two or three large NaI scintillation cameras with a detector intrinsic resolution of about 3–4 mm. In most cases, parallel-hole collimators are used whereas sporadically fan-beam collimation is applied. For the imaging of smaller objects, such as the brain, fan-beam collimators perform better than parallel-hole collimators as many more holes are directed towards the object. This results in a higher fraction of emitted gamma photons to be detected. Triple-head fan-beam systems typically reach image resolutions in the centre of the brain of 7 mm, and have a sensitivity of up to about 0.04%. However, despite their better performance, fan-beam systems are only available from a limited number of vendors.

Like SPECT, Positron emission tomography (PET) allows us to image distributions of radiolabelled molecules. While clinical PET has a better spatial resolution than currently available SPECT and is suited to image many short-living cyclotron produced isotopes, SPECT has the unique ability to image (i) many tracers with longer living isotopes and (ii) a broad variety of combinations of isotopes simultaneously. Not any of the currently used SPECT tracers do require a cyclotron at site. For a clinician the choice to perform a SPECT or a PET scan heavily depends on the availability of a SPECT or PET radio-tracer to visualize a relevant tissue property. So SPECT and PET are highly complementary techniques each with overlapping but also with unique applications.

There are definite advantages for improved human brain SPECT devices. Higher sensitivity can decrease noise and increase patient throughput, while higher resolution allows a much more localized monitoring of molecular dynamics. Together with the availability of new tracers this may significantly increase the applicability of SPECT, for (early) diagnosis and monitoring of brain diseases (Warwick 2004, Amen and Flaherty 2006).

In contrast to clinical SPECT, in small-animal SPECT sub-millimetre resolutions have become common, and recently, even sub-half-millimetre image resolutions (Beekman *et al* 2005, 2007, van der Have *et al* 2009) have been reached, despite the use of detectors with intrinsic resolutions of typically 3 mm. Detailed tracer uptake in sub-compartments of mouse organs has been visualized on a sub-millimetre scale, such as blood flow markers in the papillary muscles of a beating heart and dopamine transporter markers in tiny parts of the striatum in living mouse brain (Beekman *et al* 2005, 2007, Kim *et al* 2006, Vastenhouw *et al* 2007). Key to obtaining these ultra-high resolutions is the application of pinhole collimation. When small objects are imaged at small distances, pinhole collimation gives superior image resolution compared to parallel-hole and even fan-beam or cone-beam collimation. The

development of high-resolution detectors (Barber 1999, He *et al* 1999, Lees *et al* 2003, Fiorini *et al* 2003, Beekman and de Vree 2005, de Vree *et al* 2005, Meng 2006, Nagarkar *et al* 2006, Heemskerk *et al* 2007, Korevaar *et al* 2009) with intrinsic resolutions $\leqslant$0.5 mm is expected to result in even higher resolutions (Rogulski *et al* 1993, Beekman and Vastenhouw 2004a) and more compact devices.

Most previous studies on brain SPECT concern parallel-hole, fan-beam or cone-beam collimation. Several dedicated brain SPECT devices have been designed and constructed (Holman *et al* 1990, Zito *et al* 1993, Jin *et al* 1994, Habte *et al* 2001, Ter-Antonyan *et al* 2008). In Li *et al* (1994), Liu *et al* (1995) and Kamphuis and Beekman (1998), different geometries for brain SPECT are studied theoretically. In a few cases brain SPECT based on pinhole collimation has been investigated. Theoretical calculations and simulations of high-resolution MP-SPECT have been performed in Rowe *et al* (1993). The same group obtained reconstructed resolutions of about 5 mm using pinhole collimation and NaI detectors with an intrinsic resolution of 2.8 mm (Klein *et al* 1995). Simulations indicate that replacement of conventional detectors by high-resolution detectors can lead to reconstructed resolutions of about 2 mm (Rogulski *et al* 1993). In Mahmood *et al* (2009), a novel slit-slat collimator system is studied theoretically.

In this paper, we conduct a detailed analytical calculation of the performance of MP-SPECT dedicated to brain imaging. Our aim is twofold. The first goal is to investigate what is the optimal performance of MP-SPECT given the availability of a detector with a certain intrinsic resolution. This performance is calculated using a geometrical optimization. Our focus is on the influence of detector and collimator size, since these are the parameters that can most easily be adapted. For such an optimal system, we calculate the sensitivity and system resolution that can be reached. Second, we compare the predicted performance of MP-SPECT with that of currently used clinical devices. The comparison is made for MP-SPECT based on conventional detectors and for future systems for which we assume that high-resolution detectors will be available in sufficient amounts.

2. Methods

2.1. Analytical model

In Rentmeester *et al* (2007), an analytical model efficiently predicting the performance of MP-SPECT has been developed. This model takes into account effects such as the penetration of photons through the pinhole aperture material. Specifying a certain system resolution, it can predict the geometry of a scanner resulting in optimal sensitivity and vice versa. This model has been applied to small-animal SPECT scanners. Because for human brain imaging the system and object dimensions as well as isotope concentrations are different, dedicated optimization studies are required for clinical SPECT.

The main geometrical assumptions of the model are shown in figure 1: both the detector and collimator are modelled as spherical layers with radii r_d and r_c, respectively. In the present study, all systems under comparison have an equally-sized 'central field-of-view' (CFOV), a spherical volume of radius r_f, which is large enough to contain the entire brain. Each point in the CFOV is seen by all knife-edge pinholes (which have a physical pinhole diameter d and aperture material with attenuation coefficient μ) contained in the collimator (figure 1(b)). The actual number of pinholes that can be used is determined by the radius of the CFOV, the sizes of the detector and collimator, and the requirement that the projections of the CFOV on the detector do not overlap. The detector has an intrinsic resolution R_i and a capture efficiency ϵ. The opening angle of the detector, ω, is fixed and together with r_d determines the detector

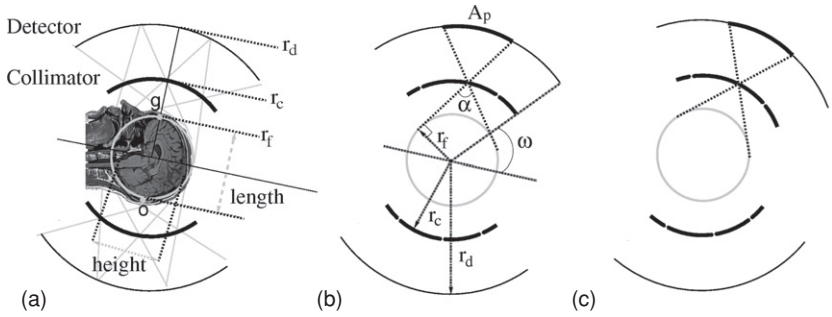

Figure 1. (a) Geometry of MP-SPECT for the human brain. The collimator and detector are modelled as spherical layers with radii r_c and r_d, respectively. The glabella (g) and occipital point (o) in the brain are shown. (b) Projection of the CFOV onto the detector via a knife-edge pinhole. (c) MP-SPECT with asymmetric detector and collimator design, to facilitate an easier entry of the head. The analytical model used in this paper is equally valid for asymmetric detectors, as long as the detector area remains the same.

area. The collimator radius r_c is always chosen in such a way that it allows for physical insertion within the detector ring as well as for the insertion of the head into the collimator. The quantities $r_f, r_c, r_d, R_i, \mu, \omega, \epsilon$ and d uniquely define the system. The opening angle α of the pinhole is always chosen just large enough for the pre-defined CFOV to be projected onto the detector without being truncated by the collimator (see figure 1). Therefore α equals $2\arcsin(r_f/r_c)$. Once the geometry and physical properties of the system are known, the size of the projection of the CFOV through one pinhole onto the detector can be calculated. This projection is a spherical cap on the detector with an area A_p of

$$A_p = 2\pi r_d \frac{r_d r_c - r_f^2 - \sqrt{\left(r_c^2 - r_f^2\right)\left(r_d^2 - r_f^2\right)}}{r_c}. \tag{1}$$

The requirement for the projections of the CFOV on the detector not to overlap implies that a certain fraction of the continuous detector surface will be covered with non-overlapping spherical cap projections. The cover fraction depends on the number of projections and for a large number of circular projections it approaches the limit $\pi/\sqrt{12}$ (Kottwitz 1991), which is the fraction that we will assume in this paper. The number of pinholes N_p in the collimator is determined by dividing the total available detector surface (the entire sphere minus two spherical caps determined by the detector opening angle ω) by A_p and taking into account the cover fraction. Consequently N_p reads

$$N_p = \frac{2\pi^2 r_d^2 \cos\omega}{\sqrt{3} A_p}. \tag{2}$$

The sensitivity of a single pinhole is calculated by assuming an isotropic propagation of the gamma radiation. Multiplication by the number of pinholes in the collimator gives the total sensitivity for a point source in the centre of the CFOV

$$S = N_p \epsilon \frac{\left(d^2 + \frac{2}{\mu} d \tan\left(\frac{\alpha}{2}\right) + \frac{2}{\mu^2}\tan^2\left(\frac{\alpha}{2}\right)\right)}{16 r_c^2}. \tag{3}$$

The system resolution reads

$$R_t = \sqrt{\left(\frac{r_c R_i}{r_c - r_d}\right)^2 + \left(\frac{r_d(d + \ln 2 \tan(\alpha/2)/\mu)}{r_c - r_d}\right)^2}. \tag{4}$$

Table 1. Parameters of the analytical model.

Symbol	Description
r_d	Radius of detector
r_c	Radius of collimator
r_f	Radius of CFOV
ϵ	Capture efficiency detector
R_i	Intrinsic detector resolution
ω	Opening angle of the detector
μ	Attenuation coefficient of the pinhole material
d	Pinhole diameter
α	Pinhole opening angle
A_p	Area of the projection of the CFOV on the detector
N_p	Number of pinholes
R_t	System resolution
S	Sensitivity

In equation (3) and (4), penetration effects through the knife-edges of the pinhole apertures are included via effective pinhole diameters, both for system resolution (Accorsi *et al* 2004) and sensitivity (Paix 1967, Metzler *et al* 2001). More details of the derivations leading to (3) and (4) can be found in Rentmeester *et al* (2007). The parameters used in this section are summarized in table 1.

2.2. Dimensions of MP-SPECT dedicated to brain imaging

For many clinical brain imaging tasks, complete images of the brain are preferred. Therefore, we choose a CFOV that contains the entire brain (figure 1(a)). In order to find a suitable value for r_f we have measured the linear dimensions of the brains of 15 adult males from MRI scans of the head. The maximum brain length was measured along the line between the glabella and the occipital point of the head, while the height is determined perpendicular to this line in the sagittal slice (see figure 1(a)). The lateral axis (width) is perpendicular to the plane formed by the lines defining length and height. The maximum values found for length, width and height were 180 mm, 145 mm and 125 mm, respectively. As there is quite a variation in these numbers we have assumed the safe value $r_f = 95$ mm for the radius of the spherical CFOV. Based on the same MRI scans, about 10 mm of fluids, bone and other tissue are estimated to be present between the outer edge of the brain and the surface of the skin. Allowing 30 mm extra space between the head and the collimator for ease of movement, we set a lower limit for the collimator radius by requiring $r_c \geqslant 135$ mm.

We assume that the collimator has gold pinhole apertures (material attenuation coefficient $\mu = 4.27$ mm^{-1} at 140 keV for ^{99m}Tc), and that the detector has a capture efficiency $\epsilon = 0.89$ and an opening angle $\omega = 45^\circ$. For $r_c = 135$ mm the port of the scanner might be too narrow to allow easy entry of the head if the geometry is as symmetrical as in figure 1(b). In reality, it would be more advantageous to tilt detector and collimator as is illustrated in figure 1(c). When the detector size remains equal, this asymmetry does not affect the validity of our equations. Another possible solution is to design a system where the upper and lower parts of the collimator can be separated to allow the head to enter.

Table 2. Parameters of the clinical systems.

	Dual-head parallel-hole	Triple-head fan-beam
Bore length	54 mm	34.9 mm
Hole diameter	2.03 mm	1.4 mm
Septal width	0.152 mm	0.15 mm
Focal length	∞	50 cm
Distance collimator to centre of rotation	13.5 cm	13.5 cm
R_t	8.0 mm	7.2 mm
S	0.017%	0.039%

2.3. Comparison with other SPECT systems

We will compare the results of our model to the performance of two presently used clinical SPECT systems. In the first setup ('DualPar') a dual-head Philips Forte scanner is used with VXHR parallel-hole collimators and 40 cm $\times$ 50 cm detectors with a 1 cm thick NaI scintillation crystal and photomultiplier tubes having an intrinsic resolution of 3.2 mm. We assume that for a brain scan the collimator surface is located at a distance of 13.5 cm from the axis of rotation of the detector heads (equal to the minimal collimator radius in MP-SPECT, see section 2.2). At this distance a system resolution of $R_t = 8.0$ mm and sensitivity $S = 0.017\%$ are calculated (Moore *et al* 1992).

The second setup ('TripleFan') is a triple-head Picker Prism 3000 XP system. The detectors (40 cm $\times$ 24 cm) are similar to those of the dual-head system, but ultra-high-resolution fan-beam collimators are used. Again we assume that the collimator surface is at 13.5 cm from the rotation axis. This device has a system resolution $R_t = 7.2$ mm and a sensitivity $S = 0.039\%$ in the centre of the field-of-view. Detailed parameters of both clinical systems are summarized in table 2. The calculated system resolutions and sensitivities are in close agreement with the values specified by the manufacturer.

3. Results

3.1. Analytical approximation

To compare the performance of MP-SPECT to conventional clinical SPECT, we either evaluate the system resolutions of the different devices at the same fixed sensitivity or we compare sensitivities at the same fixed system resolution. Fixing the sensitivity or system resolution to the desired value is accomplished by tuning the pinhole diameter. The system resolution can be expressed as a function of sensitivity and vice versa, by combining equations (3) and (4) and eliminating the pinhole diameter. The solution is given in equation (A.2).

Assuming that the model parameters $\epsilon, \omega, r_f, \mu$ and R_i are fixed, determined by the available detector and the dimensions of the human brain and head, the values of r_d and r_c giving optimal performance are calculated in the appendix. In our calculation, we have assumed that $\tan(\alpha/2)/\mu R_t \ll 1$ (the validity of the approximation is discussed in the appendix). For a system with optimal detector and collimator size we have deduced the following trade-off

relations between sensitivity and system resolution:

$$S_{\mathrm{LR}} = \frac{\epsilon\pi\cos\omega}{8\sqrt{3}r_f^2} R_{\mathrm{t,LR}}^2 \qquad \text{if} \quad \mu R_i \gg 1, \tag{5}$$

$$S_{\mathrm{HR}} = \frac{\epsilon\pi\cos\omega R_{t,\mathrm{HR}}^2}{4\sqrt{3}r_f^2\,[\mu R_i + \ln(2)]^2} \qquad \text{if} \quad \mu R_i \ll 1. \tag{6}$$

Two regimes can be identified, depending on the detector intrinsic resolution, which we denote by the low-resolution ('LR') and high-resolution ('HR') regime. Our equations are only strictly valid in the limits $\mu R_i \gg 1$ and $\mu R_i \ll 1$. To show that the equations also give an adequate description for intermediate intrinsic detector resolutions and that the approximations that we have made to arrive at these equations are justified, we have also done a numerical optimization of equation (A.2) (see the appendix). The numerical optimization comprised of (i) keeping R_t fixed and maximizing S (by varying r_d and r_c) or (ii) keeping S fixed and minimizing R_t. R_t and S were fixed at the values of the clinical reference systems (see the legend). All numerical results coincide very well with the analytical curves and we therefore conclude that for MP-SPECT dedicated to human brain imaging, equations (5) and (6) accurately describe the optimal sensitivity and system resolution that can be reached.

In the appendix, we also give expressions for the collimator and detector radii that lead to the optimal behavior described by (5) and (6). In the conventional detector limit of (5) we find that one should choose $r_d \gg r_c \gg r_f$. A large detector radius (and hence large magnification) is necessary to reduce the adverse effect of detector blurring. More surprisingly, one should also choose a collimator that is much larger than the CFOV (but much smaller than the detector). This is due to the fact that for $r_d \gg r_c \gg r_f$ the number of pinholes grows $\propto \left(r_c^2 - r_f^2/4\right)$ according to (2). Thus, although the sensitivity of a single pinhole falls off $\propto 1/r_c^2$, the combined sensitivity of all pinholes increases slightly for larger r_c. In the high-resolution detector limit of (6), the equations for optimal collimator and detector size are more involved and we refer the reader to the appendix. Clearly, in a practical geometry one cannot realize infinite detector sizes and therefore, in the following section, we will give realistic numbers for r_c and r_d that lead to close-to-optimal behaviour for a range of intrinsic detector resolutions.

Equations (5) and (6) have the form $S \propto R_t^2$, presenting a clear trade-off between system resolution and sensitivity. Such a simple sensitivity-system resolution trade-off can serve as a useful guide for system design: when a certain improvement factor x in system resolution is desired, one will have to sacrifice approximately a factor x^2 in sensitivity (if the detector intrinsic resolution is not improved). The proportionality constant between S and R_t^2 has the largest value in equation (6), meaning that, not very surprisingly, high-resolution detectors improve system performance. The two asymptotes of (5) and (6) cross when $\mu R_i = 0.7$. For gold pinholes, the cross-over occurs when $R_i \simeq 0.2$ mm. Detectors that are typically used in the clinic have $R_i \approx 3$ mm and therefore fall into the low-resolution regime of equation (5).

By taking the limit $R_i \to 0$ the relation between the theoretically maximally attainable sensitivity and best system resolution is described by

$$S_{\max} = \frac{\epsilon\pi\cos\omega}{4\sqrt{3}r_f^2\ln^2(2)} R_{t,opt}^2 = 4.2 S_{\mathrm{LR}}. \tag{7}$$

Therefore, the application of high-resolution detectors instead of conventional gamma-cameras in optimized MP-SPECT can at most lead to a sensitivity increase by a factor of 4.2 (at fixed resolution) or an improvement in system resolution with a factor of 2.0 (at fixed sensitivity).

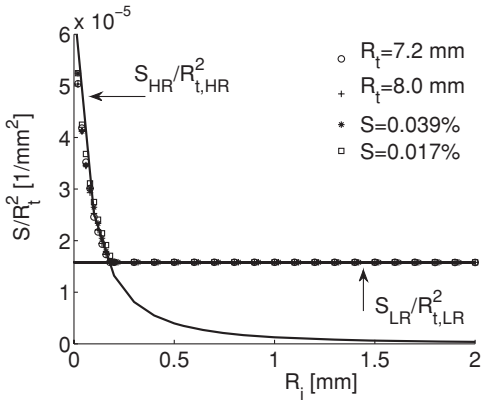

Figure 2. Optimized ratio S/R_t^2 versus intrinsic detector resolution R_i. The datapoints represent numerical optimizations, either optimized by maximizing S (with respect to r_d and r_c) at fixed system resolutions $R_t = 7.2$ mm and $R_t = 8.0$ mm, or by minimizing the value of R_t (also with respect to r_d and r_c) at fixed sensitivities $S = 0.039\%$ and $S = 0.017\%$. The analytical approximations $S_{\mathrm{HR}}/R_{t,\mathrm{HR}}^2$ and $S_{\mathrm{LR}}/R_{t,\mathrm{LR}}^2$ (solid lines) describe the data well in the appropriate regimes.

3.2. Comparison with clinical systems

In the previous section, we have described the optimal sensitivities and system resolutions that can be obtained using MP-SPECT. In this section, we compare these optimal values with the sensitivities of the clinical devices and we give numbers for the collimator and detector radii that one should choose to have close-to-optimal behavior (defined to be 90% of the optimal sensitivities/system resolutions).

In figures 3 and 4, the system resolution R_t, number of pinholes N_p and the pinhole diameter d of MP-SPECT with fixed collimator size $r_c = 180$ mm are shown as a function of r_d for various values of detector intrinsic resolution R_i. The sensitivity is kept fixed at 0.017% (equal to DualPar, figure 3) and 0.039% (TripleFan, figure 4), respectively. The analytical approximations of (5) and (7) are displayed as well. Note that in this figure r_c is fixed and it is not set to its optimal value (which depends on R_i and would be different for every curve). However, we find that this figure illustrates the dependence of system resolution on detector radius well. The improvement factors that we will mention are for a fully optimized system (i.e. a system with optimal collimator and detector radius) and these improvement factors as well as the collimator and detector sizes necessary to reach 90% of these improvements are summarized in table 3. For $R_i \geqslant 0.5$ mm (i.e. within the low-resolution detector regime of equation (5)) the curves approach the analytical expression for $R_{\mathrm{t,LR}}$ for large r_d. We calculate $R_{\mathrm{t,LR}} = 3.3$ mm (for $S = 0.017\%$) and $R_{\mathrm{t,LR}} = 5.0$ mm ($S = 0.039\%$), an improvement with factors of 2.4 and 1.4 compared to DualPar and TripleFan, respectively. For $S = 0.017\%$, the minimally required detector radius to achieve a close-to-optimal resolution is calculated to be $r_d = 721, 599, 475, 343$ and 266 mm for $R_i = 4, 3, 2, 1$ and 0.5 mm respectively; for $S = 0.039\%$ these values read $r_d = 583, 497, 408, 313$ and 256 mm, respectively. For $R_i = 0.15$ mm, which falls on the boundary of the two R_i regimes, an improvement in resolution by a factor of 2.6 (DualPar) and 1.5 (TripleFan) can be reached. For $R_i = 0.05$ mm (i.e. the high-resolution detector regime) the system performance increases enormously and the system resolution can be improved by factors of 3.8 and 2.3 compared to DualPar and

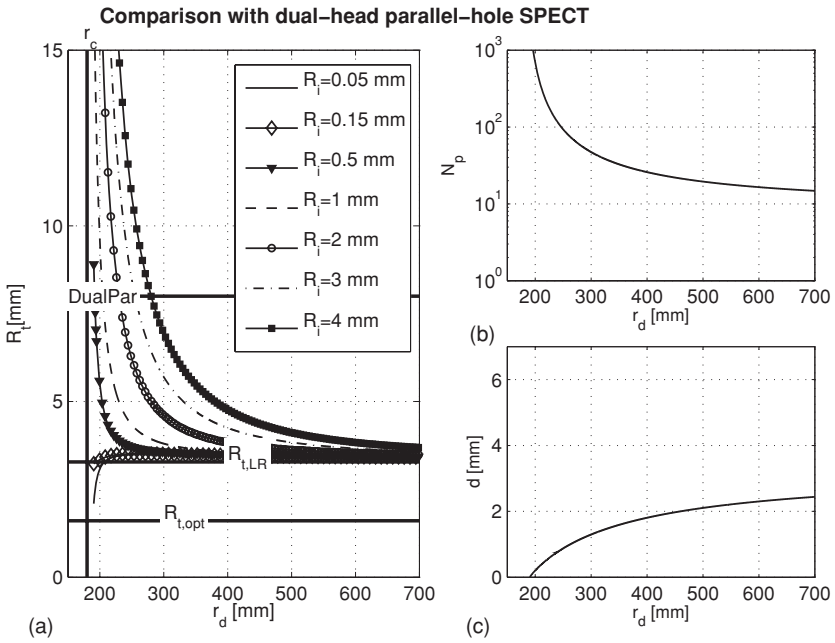

Figure 3. (a) System resolution R_t versus detector radius r_d of MP-SPECT (inverse of equation (A.2)) for detector intrinsic resolutions $R_i = 0.05, 0.15, 0.5, 1, 2, 3$ and 4 mm and fixed sensitivity $S = 0.017\%$ (value of clinical parallel-hole device). The horizontal lines show the values of the clinical dual-head parallel-hole device ('DualPar') and the analytical predictions $R_{t,\mathrm{LR}}$ (equation (5)) and $R_{t,\mathrm{opt}}$ (equation (7)). The collimator radius is fixed at $r_c = 180$ mm, while $\epsilon = 0.89$, $r_f = 95$ mm, $\omega = 45°$, $\mu = 4.27$ mm^{-1}. (b) Number of pinholes N_p versus r_d for the same parameters. (c) Pinhole diameter versus r_d for the same parameters.

TripleFan. In this case a detector radius of 146 mm and 150 mm (for S fixed at 0.017% and $S = 0.039\%$) are close-to-optimal. Whereas in the conventional detector regime a larger detector radius (and thus higher magnification) leads to better performance, here the opposite effect occurs: a smaller detector radius (and de-magnification) gives better results.

In figures 5 and 6, the sensitivity of the MP-SPECT system is displayed as a function of r_d, with R_t being fixed to 8.0 mm (DualPar, figure 5) and 7.2 mm (TripleFan, figure 6) and fixed collimator size $r_c = 180$ mm. As for the system resolution, sensitivity improvement factors and collimator and detector radii necessary to reach close-to-optimal sensitivity are summarized in table 3. Compared to DualPar and TripleFan, improvements in sensitivity by factors of 6.0 and 2.1 are possible for $R_i \geqslant 0.5$ mm (i.e. detectors within the low-resolution detector regime). For $R_i = 0.15$ mm the improvement factors increase to 6.7 and 2.4, respectively. The sensitivity increases enormously for $R_i = 0.05$ mm (i.e. a detector within the high-resolution detector regime) to factors of 14.5 (compared to DualPar) and 5.1 (compared to TripleFan). For the low-resolution detector regime, the optimal sensitivities are obtained (within 90%) at detector radii of $r_d = 787, 674, 557, 430$ and 354 mm for $R_i = 4, 3, 2, 1$ and 0.5 mm, respectively, when R_t is fixed to a value of 8.0 mm, while for $R_t = 7.2$ mm the respective detector radii read $r_d = 842, 716, 586, 446$ and 363 mm. For $R_i = 0.15$ mm the detector radii that give close-to-optimal performance are 139 mm and 140 mm (for $R_t = 8.0$ mm and $R_t = 7.2$ mm, respectively), while for $R_i = 0.05$ mm the respective detector radii become 156 and 154 mm. Figures 3–6 show that the number of pinholes decreases with increasing

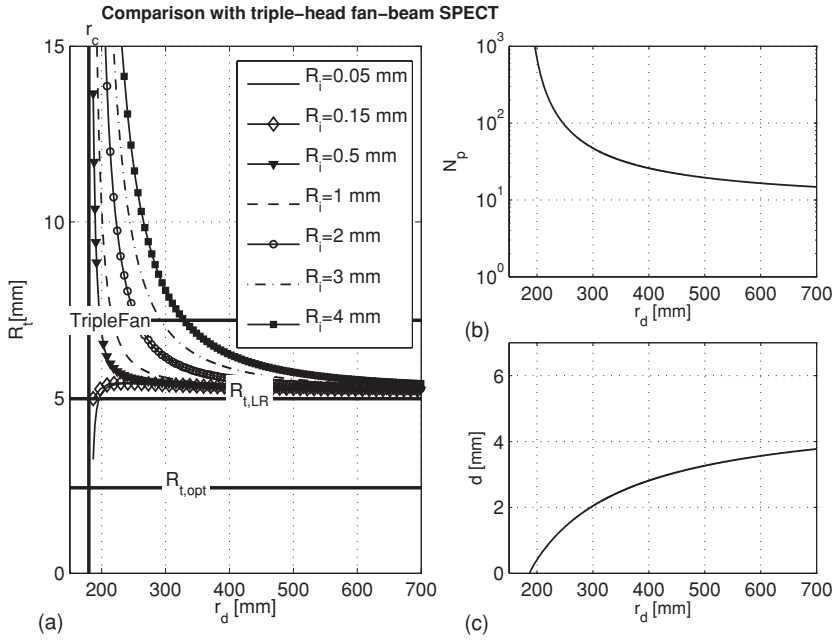

Figure 4. The same as figure 3 but with sensitivity fixed at $S = 0.039\%$ (value of clinical fan-beam device, 'TripleFan').

detector radius r_d. For rather large detector radii (as required for $R_i \geqslant 0.5$ mm) the number of pinholes is rather low. However, the number of pinholes has to be large enough to allow for sufficient angular sampling, which means that small translations or a few rotations are necessary.

4. Discussion

Using analytical modelling, we have calculated the optimal performance of MP-SPECT dedicated to brain imaging. We find that the trade-off between sensitivity and system resolution of optimized MP-SPECT has the form $S \propto R_t^2$. This proportionality can serve as a simple rule of thumb in system design: it tells us how much we have to sacrifice in sensitivity if we want to improve system resolution and vice versa (assuming that the intrinsic detector resolution R_i remains constant). Our theory predicts that the required size of the detector to obtain a high performance depends on R_i. For detector intrinsic resolutions $\mu R_i > 0.7$ (typically $R_i > 0.2$ mm), the optimal detector radius is large, resulting in a magnified object projection onto the detector, thus reducing the image degrading effect of detector blurring. In this regime, the performance of MP-SPECT is almost independent of R_i. However, improving R_i is still beneficial because it will reduce the required detector area. Dramatically different behavior occurs for $\mu R_i < 0.7$. In this regime, MP-SPECT performance can be tremendously improved by placing the detector close to the collimator: the large number of pinholes more than compensates for the increased effect of detector blurring, as is apparent from figure 2. The latter idea was already put forward in Rogulski *et al* (1993) although it was not quantified at the time.

Table 3. Improvement factors of MP-SPECT compared to clinical SPECT and collimator and detector radii sufficient to reach 90% of this improvement.

Comparison to dual-head parallel-hole device						
	R_t (at equal $S = 0.017\%$)			S (at equal $R_t = 8.0$ mm)		
R_i (mm)	System resolution improvement	r_c (mm)	r_d (mm)	Sensitivity improvement	r_c (mm)	r_d (mm)
4	2.4	155	721	6.0	227	787
3	2.4	157	599	6.0	229	674
2	2.4	161	475	6.0	235	557
1	2.4	167	343	6.0	244	430
0.5	2.4	171	266	6.0	251	354
0.15	2.6	135	146	6.7	135	139
0.05	3.8	135	146	14.5	153	156
Comparison to triple-head fan-beam device						
	R_t (at equal $S = 0.039\%$)			S (at equal $R_t = 7.2$ mm)		
R_i (mm)	System resolution improvement	r_c (mm)	r_d (mm)	Sensitivity improvement	r_c (mm)	r_d (mm)
4	1.4	165	583	2.1	224	842
3	1.4	168	497	2.1	229	716
2	1.4	171	408	2.1	234	586
1	1.4	179	313	2.1	244	446
0.5	1.4	182	256	2.1	251	363
0.15	1.5	135	142	2.4	135	140
0.05	2.3	143	150	5.1	151	154

We have found that an optimized MP-SPECT system has great potential to improve clinical brain SPECT. A comparison with conventional clinical systems has shown that when detectors with intrinsic resolutions $R_i \geqslant 0.5$ mm are used, system resolutions can be improved by factors of 2.4 and 1.4 (at equal sensitivity) compared to DualPar and TripleFan, respectively. At equal system resolution, the respective improvements in sensitivity are 6.0 and 2.1. Using high-resolution detectors ($R_i = 0.05$ mm) vast improvements of the resolution by factors of 3.8 and 2.3 and of the sensitivity by factors of 14.5 and 5.1 are within reach. Detectors with resolutions down to 0.05 mm have been developed recently (e.g. de Vree *et al* 2005, Beekman and de Vree 2005, Meng 2006, Nagarkar *et al* 2006). At present, however, these detectors have rather low capture efficiencies. For high-energy gamma detection the challenge remains to augment the efficiency while preserving the resolution (Barber 1999, He *et al* 1999, Lees *et al* 2003, Fiorini *et al* 2003, de Vree *et al* 2005, Meng 2006, Nagarkar *et al* 2006, Heemskerk *et al* 2007, Korevaar *et al* 2009).

Note that when placing the detector closely to the pinhole centres (as required for high-resolution detectors), the collimator walls should be thin enough to allow for this. In this paper, we have neglected direct penetration of gamma rays through the collimator which implies that a certain wall thickness is required. For ^{99m}Tc a wall thickness of several millimetres is sufficient and this does not pose problems with the geometries considered in this paper (see table 3). For higher energy isotopes, an asymmetrical placement of the pinhole centres in the collimator wall can possibly solve this issue.

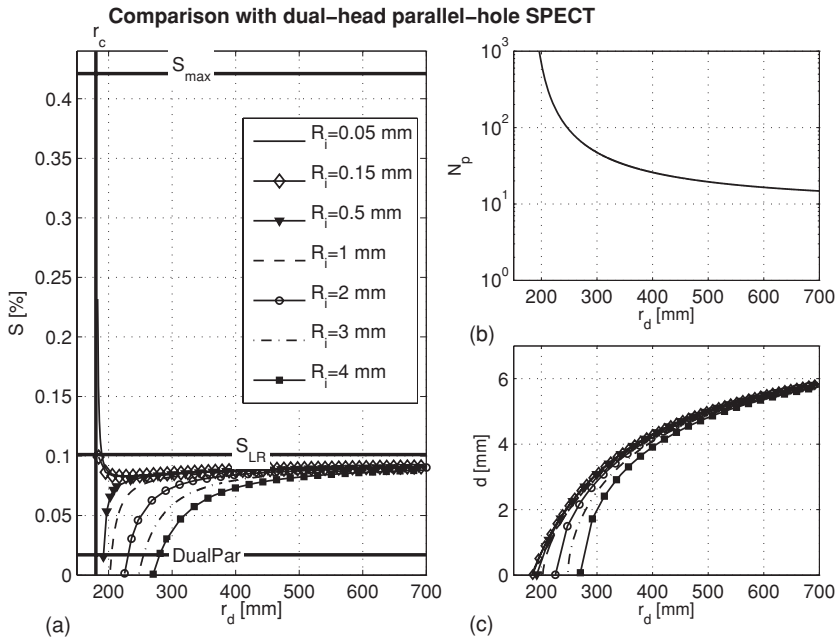

Figure 5. (a) Sensitivity S versus detector radius r_d of MP-SPECT (equation (A.2)) for detector intrinsic resolutions $R_i = 0.05, 0.15\,0.5, 1, 2, 3$ and 4 mm and fixed system resolution $R_t = 8.0$ mm (value of clinical parallel-hole device). The horizontal lines show the values of the clinical dual-head parallel-hole device ('DualPar') and the analytical predictions S_{LR} (equation (5)) and $S_{\max}$ (equation (7)). The collimator radius is fixed at $r_c = 180$ mm, while $\epsilon = 0.89$, $r_f = 95$ mm, $\omega = 45^\circ$, $\mu = 4.27$ mm^{-1}. (b) Number of pinholes N_p versus r_d for the same parameters. (c) Pinhole diameter versus r_d for the same parameters.

In this paper, we consider the system resolution and sensitivity as the parameters that characterize system performance. The final image resolution that can be obtained with a certain system will in principle depend on the full shape of the system's response and not only on the system resolution, which is a measure of the full width at half-maximum of that response. Furthermore, the expressions for sensitivity and system resolution that we use are only strictly valid in the centre of the CFOV. At other positions, the distance to some pinholes is smaller than r_c, while the distance to other pinholes is larger and the source can be off-axis with regard to the pinholes. To check if the values in the centre represent a good average, we have calculated the system resolution and sensitivity over the whole CFOV for several optimized MP-SPECT designs and we find only slight variations. We plan to take these issues further into account in future work by considering simulated images of human brain SPECT for a range of parameters.

Aspects which are beyond the scope of the model and have not been taken into account, could lead to even better results. We have assumed a safe value $r_f = 95$ mm for the field-of-view radius, but since the width and height of the brain are smaller (cf figure 1(a)), a more elliptically shaped collimator could be used with on average a smaller radius r_c, leading to better performance. Also, a helmet design such as used in Rowe *et al* (1993) can be more optimal than the spherical shells assumed in this paper. Finally, with the aid of special focusing techniques, such as used in the U-SPECT scanners, a higher sensitivity might be obtained, as well as a better system resolution (Beekman 2002, Beekman *et al* 2004b). This could be

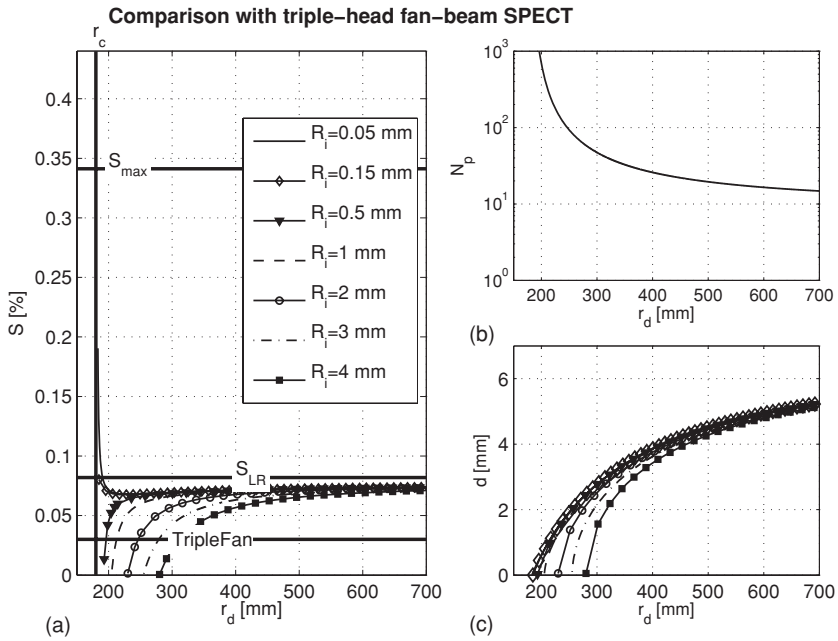

Figure 6. The same as figure 5, but with system resolution fixed at $R_t = 7.2$ mm (value of clinical fan-beam device, 'TripleFan').

advantageous, for example, when only a small region of the brain needs to be imaged at a high resolution. For whole-brain imaging, however, it implies the need for a sufficiently large collimator, either to accommodate the whole brain within the CFOV, or to leave room to move the pinhole focus through the entire head (Vastenhouw and Beekman 2007). Movements of the collimator can also be used to augment the CFOV above the 95 mm radius that is assumed in this paper, which is desired for some applications (Matsuda *et al* 1992). Note that most (but not all) of the optimal collimator sizes of the geometries in this paper allow some room for extra collimator movements (see table 3).

5. Conclusion

In this paper, the system resolution and sensitivity of MP-SPECT dedicated to human brain imaging have been studied using an analytical pinhole collimation model. Even when the setup employs conventional detectors, MP-SPECT systems can achieve significant improvements in system resolution over resolutions found in presently used clinical SPECT devices when compared at equal sensitivity; likewise, improvements in sensitivity at fixed system resolution are possible. The performance is improved tremendously when high-resolution detectors (typically $R_i < 0.2$ mm) replace the conventional detectors.

Our results support the idea that an optimal combination of multi-pinhole collimation and high-resolution detectors will improve system performance of future clinical SPECT. This will benefit patient throughput, patient comfort, dynamic imaging capabilities and image quality aspects.

Acknowledgments

We would like to thank Dr F van der Have, J W T Heemskerk, J Huybregts, R Koppel, Dr T Roeling and Dr T C de Wit for valuable discussions. This work was sponsored by IOP photonics grant IPD067766.

Appendix. Analytical derivation

This appendix provides the details of the derivation leading to equations (5) and (6). Let us first combine the equations of section 2.1 to express the sensitivity and system resolution in terms of all model parameters. Equations (1)–(3) give a sensitivity of

$$S = \frac{\epsilon\pi r_d \cos(\omega)}{16\sqrt{3}r_c\left(r_d r_c - r_f^2 - \sqrt{\left(r_c^2 - r_f^2\right)\left(r_d^2 - r_f^2\right)}\right)} \times \left(d^2 + d\frac{2}{\mu}\tan(\alpha/2) + \frac{2}{\mu^2}\tan^2(\alpha/2)\right). \tag{A.1}$$

The pinhole diameter d is chosen in such a way that either the sensitivity or the system resolution is set to the desired fixed value. We can express the sensitivity S as a function of system resolution R_t by combining equation (4) and (A.1) and eliminating d. We find

$$S = \frac{\epsilon\pi \cos(\omega)}{16\sqrt{3}\mu^2 r_c r_d\left(r_c r_d - r_f^2 - \sqrt{\left(r_c^2 - r_f^2\right)\left(r_d^2 - r_f^2\right)}\right)} \times \left[\mu^2\left((r_d - r_c)^2 R_t^2 - r_c^2 R_i^2\right) + r_d^2(2 + \ln^2 2 - \ln 4)\tan^2\left(\frac{\alpha}{2}\right) - 2\mu r_d\sqrt{(r_d - r_c)^2 R_t^2 - r_c^2 R_i^2}(-1 + \ln 2)\tan\left(\frac{\alpha}{2}\right)\right]. \tag{A.2}$$

This equation can be inverted if one wants to express R_t as a function of S. A comment about the limit $r_d \to r_c$ should be made. From (A.2) it would seem as if the sensitivity would diverge in this limit. This is due to the fact that in this limit (1) predicts that the projections of the CFOV onto the detector have an area of zero, and therefore an infinite number of pinholes can be used according to (2). It is clear that our analytical model is not valid in such an unrealistic limit. In fact, (1) assumes that the size of the projection exceeds the magnified pinhole area $(r_d - r_c)\pi d^2/(4r_d)$ which is the case in all situations described in this paper.

Equation (A.2) describes the behavior of the system and can in principle be used to calculate optimal parameter values. However, the resulting equations are long and not very insightful. To be able to write the results in a more simple form we introduce a parameter

$$\delta \equiv \tan(\alpha/2)/(\mu R_t). \tag{A.3}$$

With this new parameter we can rewrite (A.2) as

$$S = \frac{\epsilon\pi \cos(\omega)\tan^2(\frac{\alpha}{2})}{16\sqrt{3}\mu^2 r_c r_d\left(r_c r_d - r_f^2 - \sqrt{\left(r_c^2 - r_f^2\right)\left(r_d^2 - r_f^2\right)}\right)} \times \left[\left(\frac{r_d - r_c}{\delta}\right)^2 - \left(\frac{r_c\mu R_i}{\tan(\alpha/2)}\right)^2 + r_d^2(2 + \ln^2 2 - \ln 4) - 2r_d\sqrt{\left(\frac{r_d - r_c}{\delta}\right)^2 - \left(\frac{r_c\mu R_i}{\tan(\alpha/2)}\right)^2}(-1 + \ln 2)\right]. \tag{A.4}$$

The calculation outlined in the remainder of this appendix is done without any approximations, but when writing down the results, we perform a Taylor expansion in terms of δ and we only give the leading order in δ. These approximative formulae will be accurate if $\delta \ll 1$. Being limited to $r_c > 135$ mm and $r_f = 95$ mm and assuming gold pinholes (see section 2) we find that $\tan(\alpha/2)/\mu < 0.23$ mm. Our approximate equations are therefore expected to hold for system resolutions $R_t \gg 0.23$ mm. Since we are comparing MP-SPECT with clinical devices having system resolutions >7 mm we expect that our approximation will hold (and this is also shown in the paper, see figure 2).

We start with optimizing sensitivity for a fixed system resolution, i.e. R_t is kept fixed, while S may vary as a function of r_d. In this case, we are interested in the detector radius $r_{d,\mathrm{opt}}$ which maximizes S. For such a maximization we first determine the allowed range of r_d. In principle, there is no upper limit on r_d, but there is a lower limit. When r_d is decreased, the effect of detector blurring increases and a reduction in diameter d is necessary to keep R_t fixed. Of course, we are limited by the physical requirement $d > 0$. Taking the limit $d \to 0$ in equation (4) and solving for r_d gives us the minimal detector radius $r_{\min}$. An expansion to first order in $\delta = \tan(\alpha/2)/(\mu R_t)$ yields

$$r_{\min} = r_c \left(1 + \delta \sqrt{\left(\frac{\mu R_i}{\tan(\alpha/2)} \right)^2 + \ln^2 2} \right). \tag{A.5}$$

So let us calculate the sensitivity in the limiting cases of $r_d \to \infty$ and $r_d \to r_{\min}$. Up to leading order in δ we find

$$\begin{aligned} \lim_{r_d \to r_{\min}} S &= \frac{\epsilon\pi \cos\omega \tan^2(\alpha/2)}{4\sqrt{3}\mu^2\delta^2 r_f^2 \left(\left(\frac{\mu R_i}{\tan(\alpha/2)} \right)^2 + \ln^2(2) \right)} \cos^2(\alpha/2) \\ &= \frac{\epsilon\pi \cos\omega R_t^2}{4\sqrt{3} r_f^2 \left(\left(\frac{\mu R_i}{\tan(\alpha/2)} \right)^2 + \ln^2(2) \right)} \cos^2(\alpha/2), \end{aligned} \tag{A.6}$$

$$\begin{aligned} \lim_{r_d \to \infty} S &= \frac{\epsilon\pi \cos\omega \tan^2(\alpha/2)}{8\sqrt{3}\mu^2\delta^2 r_f^2} \cos^2(\alpha/4) \\ &= \frac{\epsilon\pi \cos\omega R_t^2}{8\sqrt{3} r_f^2} \cos^2(\alpha/4). \end{aligned} \tag{A.7}$$

Now that we have found expressions for S at the borders of the allowed interval for r_d, we have to find out if there is a local maximum in S in the range $r_d \in [r_{\min}, \infty]$. We therefore solve $\partial S/\partial r_d = 0$. We find a solution for

$$r_{d,loc} = r_c \left[1 + \delta \frac{\sqrt{q\left(-2 + q + x^2 - \ln^2 2 + \ln 4\right)}}{\sqrt{2}(1 - \ln 2)} \right], \tag{A.8}$$

with

$$x = \frac{\mu R_i}{\tan(\alpha/2)}, \tag{A.9}$$

$$q = \sqrt{x^4 + 2x^2(-2 + \ln 2)\ln 2 + (2 + \ln^2 2 - \ln 4)^2}. \tag{A.10}$$

We will not continue to give the full expression for S at $r_d = r_{d,\mathrm{loc}}$, but we will prove that in the limiting cases $\mu R_i \ll 1$ and $\mu R_i \gg 1$, equations (A.6) and (A.7) describe the maximum of S. First for $\mu R_i / \tan(\alpha/2) \ll 1$ we find

$$\lim_{\mu R_i / \tan(\alpha/2) \to 0} r_{d,loc} = r_c < r_{\min}. \tag{A.11}$$

So for detectors with $\mu R_i / \tan(\alpha/2) \ll 1$ (high-resolution detectors), $r_{d,loc}$ does not lie in the allowed interval and is therefore not an allowed physical solution. In this case, the maximum is at $r_d = r_{\min}$ since for $R_i \to 0$ the value of S at $r_d = r_{\min}$ (A.6) is larger than the value for S in the limit $r_d \to \infty$ (A.7). Second, we consider the limit $\mu R_i / \tan(\alpha/2) \gg 1$. In that limit we calculate

$$\lim_{\mu R_i / \tan(\alpha/2) \to \infty} r_{d,loc} = \infty. \tag{A.12}$$

We therefore find that for large $\mu R_i / \tan(\alpha/2)$ a large detector radius $r_d \gg r_c$ maximizes S.

To summarize, we have determined the maximal sensitivity of equation (A.2) with respect to r_d for the limiting cases $\mu R_i / \tan(\alpha/2) \ll 1$ and $\mu R_i / \tan(\alpha/2) \gg 1$, keeping only the leading order in the quantity $\delta = \tan(\alpha/2)/(\mu R_t)$. Although our derivation does not make any statements about the intermediate regime, we find numerically that the two asymptotes that we have calculated do actually give an accurate description of the system performance for all values of R_i (see figure 2) for human brain SPECT.

Now that we have determined the optimal value of r_d in two different limits, we will also calculate the optimal collimator radius $r_{c,opt}$ in the same limits. This optimal collimator radius can be determined straightforwardly from equations (A.6) and (A.7). Note that r_c is present in these equations via the opening angle $\alpha = 2\arcsin(r_f/r_c)$. For $\mu R_i / \tan(\alpha/2) \ll 1$ equation (A.6) describes the sensitivity. Solving $\partial S/\partial r_c = 0$ gives $r_{c,\mathrm{opt}} = r_f\sqrt{1 + \ln 2/(\mu R_i)}$. In this case, the condition $\mu R_i / \tan(\alpha/2) \ll 1$ reduces to $\mu R_i \ll 1$. For $\mu R_i / \tan(\alpha/2) \gg 1$, the sensitivity in (A.7) is maximized for $\cos(\alpha/4) \to 1$, i.e. for $r_c \gg r_f$. In the derivation of equation (A.7) we have already assumed $r_d \gg r_c$ and one should therefore choose $r_d \gg r_c \gg r_f$. In this limit the condition $\mu R_i / \tan(\alpha/2) \gg 1$ reduces to $\mu R_i \gg 1$. Putting $r_{c,opt}$ in equation (A.6) and (A.7) we find

$$\max[S] = \frac{\epsilon\pi \cos\omega R_t^2}{8\sqrt{3} r_f^2} \qquad \text{for} \quad \mu R_i \gg 1, \tag{A.13}$$

$$\max[S] = \frac{\epsilon\pi \cos\omega R_t^2}{4\sqrt{3} r_f^2 (\mu R_i + \ln(2))^2} \qquad \text{for} \quad \mu R_i \ll 1. \tag{A.14}$$

Note that (A.13) and (A.14) are equal to equations (5) and (6) given in the main body of the paper.

A completely equivalent derivation can be carried out to find the best value of R_t, with S being fixed. We will not repeat the derivation here, but merely mention that within our approximations it gives the same results for the optimal value of r_d and the trade-off relations of equations (A.13) and (A.14) remain valid.

References

Accorsi R and Metzler S D 2004 Analytic determination of the resolution-equivalent effective diameter of a pinhole collimator *IEEE Trans. Med. Imaging* **23** 750–63

Amen D G and Flaherty L T 2006 Is brain imaging clinically useful for psychiatrists? *Clin. Psychiatry News* **34** 11

Barber H B 1999 Applications of semiconductor detectors to nuclear medicine *Nucl. Instrum. Methods* A **436** 102–10

Beekman F J 2002 A method for obtaining a tomographic image including an apparatus *Patent Application* PCT/NL02/00303 (May 8)

Beekman F J and de Vree G A 2005 Photon-counting versus an integrating CCD-based gamma camera: important consequences for spatial resolution *Phys. Med. Biol.* **50** N109–N119

Beekman F J and van der Have F 2007 The pinhole: gateway to ultra-high-resolution three-dimensional radionuclide imaging *Eur. J. Nucl. Med. Mol. Imaging* **34** 151–61

Beekman F J, van der Have F, Vastenhouw B, van der Linden A J A, van Rijk P P, Burbach J P H and Smidt M P 2005 U-SPECT I: a novel system for submillimeter-resolution tomography with radiolabeled molecules in mice *J. Nucl. Med.* **46** 1194–200

Beekman F J and Vastenhouw B 2004a Design and simulation of a high-resolution stationary SPECT system for small animals *Phys. Med. Biol.* **49** 4579–92

Beekman F J, Vastenhouw B and van der Have F 2004b Towards 3D nuclear microscopy using locally focusing many-pinhole SPECT *Proc. 2003 Int. Meeting on Fully Three-dimensional Image Reconstruction in Radiology and Nuclear Medicine*

Borroni B *et al* 2006 Combined ^{99m}Tc-ECD SPECT and neuropsychological studies in MCI for the assessment of conversion to AD *Neurobiol. Aging* **27** 24–31

de Vree G A, Westra A H, Moody I, van der Have F, Ligtvoet K M and Beekman F J 2005 Photon-counting gamma camera based on an electron-multiplying CCD *IEEE Trans. Nucl. Sci.* **52** 580–8

Fiorini C, Longoni A, Perotti F, Labanti C, Rossi E, Lechner P, Soltau H and Struder L 2003 A monolithic array of silicon drift detectors coupled to a single scintillator for gamma-ray imaging with sub-millimeter position resolution *Nucl. Instrum. Methods* A **512** 265–71

Habte F, Stenstrom P, Rillbert A, Bousselham A, Bohm C and Larsson S A 2001 A cylindrical SPECT camera with de centralized readout scheme *Nucl. Instrum. Methods* A **471** 80–4

He Z, Li W, Knoll G F, Wehe D K, Berry J and Stahle C M 1999 3-D position sensitive CdZnTe gamma-ray spectrometers *Nucl. Instrum. Methods* A **422** 173–8

Heemskerk J W T, Westra A H, Linotte P M, Ligtvoet K M, Zbijewski W and Beekman F J 2007 Front-illuminated versus back-illuminated photon-counting CCD-based gamma camera: important consequences for spatial resolution and energy resolution *Phys. Med. Biol.* **52** N149–62

Holman B L, Carvalho P A, Zimmerman R E, Johnson K A, Tumeh S S, Smith A P and Genna S 1990 Brain perfusion SPECT using an annular single-crystal camera-initial clinical-experience *J. Nucl. Med.* **31** 1456–61

Jin Y, Liu J, Chang W, Xu X, Liu Y and Huang G 1994 Calibration and correction of a modular cylindrical SPECT system (McSPECT II) *Nuclear Science Symp. and Medical Imaging Conf., IEEE Conf. Record* vol 4 pp 1777–80

Kamphuis C and Beekman F J 1998 The use of offset cone-beam collimators in a dual head system for combined emission transmission brain SPECT: a feasibility study *IEEE Trans. Nucl. Sci.* **45** 1250–4

Kim H, Furenlid L R, Crawford M J, Wilson D W, Barber H B, Peterson T E, Hunter W C J, Liu Z L, Woolfenden J M and Barrett H H 2006 SemiSPECT: a small-animal single-photon emission computed tomography (SPECT) imager based on eight cadmium zinc telluride (CZT) detector arrays *Med. Phys.* **33** 465–74

Klein W P, Barrett H H, Pang I W, Patton D D, Rogulski M M, Sain J D and Smith W E 1995 FASTSPECT: electrical and mechanical design of a high-resolution dynamic SPECT imager *Nuclear Science Symp. and Medical Imaging Conf., IEEE Conf. Record* vol 2 pp 931–3

Kottwitz D A 1991 The densest packing of equal circles on a sphere *Acta Cryst.* A **47** 158–65

Korevaar M A N, Heemskerk J W T, Goorden M C and Beekman F J 2009 Multi-scale algorithm for improved scintillation detection in a CCD based gamma camera *Phys. Med. Biol.* **54** 831–42

Kung M P, Hou C, Zhuang Z P, Skovronsky D and Kung H F 2004 Binding of two potential imaging agents targeting amyloid plaques in postmortem brain tissues of patients with Alzheimer's disease *Brain Res.* **1025** 98–105

Lees J E, Fraser G W, Keay A, Bassford D, Ott R and Ryder W 2003 The high resolution gamma imager (HRGI): a CCD based camera for medical imaging *Nucl. Instrum. Methods* A **513** 23–6

Li J Y, Jaszczak R J, Turkington T G, Metz C E, Gilland D R, Greer K L and Coleman R E 1994 An evaluation of lesion detectability with cone-beam fanbeam and parallel-beam collimation in SPECT by continuous ROC study *J. Nucl. Med.* **35** 135–40

Liu J G, Chang W and Loncaric S 1995 Comparison of different imaging geometries of brain SPECT systems *IEEE Trans. Nucl. Sci.* **42** 1147–53

Mahmood S T, Erlandsson K, Cullum I and Hutton B F 2009 Design of a novel slit-slat collimator system for SPECT imaging of the human brain *Phys. Med. Biol.* **54** 3433–49

Matsuda H, Tsuji S, Shuke N, Sumiya H, Tonami N and Hisada K 1992 A quantitative approach to technetium-99m hexamethylprpylene amine oxime *J. Nucl. Med.* **19** 195–200

McKeith I *et al* 2007 Sensitivity and specificity of dopamine transporter imaging with ^{123}I-FP-CIT SPECT in dementia with Lewy bodies: a phase III, multicentre study *Lancet Neurol.* **6** 305–13

Meng L J 2006 An intensified EMCCD camera for low energy gamma ray imaging applications *IEEE Trans. Nucl. Sci.* **53** 2376–84

Metzler S D, Bowsher J E, Smith M F and Jaszczak R J 2001 Analytic determination of pinhole collimator sensitivity with penetration *IEEE Trans. Med. Imaging* **20** 730–41

Moore S C, Kouris K and Cullum I 1991 Collimator design for single photon emission tomography *Eur. J. Nucl. Med.* **19** 138–50

Nagarkar V V, Shestakova I, Gaysinskiy V, Singh B, Miller B W and Barber H B 2006 Fast x-ray/γ-ray imaging using electron multiplying CCD-based detector *Nucl. Instrum. Methods* A **563** 45–8

Newberg A B, Wintering N A, Plössl K, Hochold J, Stabin M G, Watson M, Skovronsky D, Clark C M, Kung M P and Kung H F 2007 Safety, biodistribution, and dosimetry of ^{123}I IMPY: a novel amyloid plaque-imaging agent for the diagnosis of Alzheimer's disease *J. Nucl. Med.* **47** 748–54

Nordberg A 2004 PET imaging of amyloid in Alzheimer's disease *Lancet Neurol.* **3** 519–27

Paix D 1967 Pinhole imaging of gamma rays *Phys. Med. Biol.* **12** 489–500

Rentmeester M C M, van der Have F and Beekman F J 2007 Optimizing multi-pinhole SPECT geometries using an analytical model *Phys. Med. Biol.* **52** 2567–81

Rogulski M M, Barber H B, Barrett H H, Shoemaker R L and Woolfenden J M 1993 Ultra-high-resolution brain SPECT imaging: simulation results *IEEE Trans. Nucl. Sci.* **40** 1123–9

Rowe R K, Aarsvold J N, Barrett H H, Chen J C, Klein W P, Moore B A, Pang I W, Patton D D and White T A 1993 A stationary hemispherical SPECT imager for three-dimensional brain imaging *J. Nucl. Med.* **34** 474–80

Ter-Antonyan R, Jaszczak R J, Bowsher J E, Greer K L and Metzler S D 2008 Quantitative evaluation of half-cone-beam scan paths in triple-camera brain SPECT *IEEE Trans. Nucl. Sci.* **55** 2518–26

Van der Have F, Vastenhouw B, Ramakers R M, Branderhorst W, Krah J O, Ji C, Staelens S G and Beekman F J 2009 U-SPECT II: an ultra-high-resolution device for molecular small-animal imaging *J. Nucl. Med.* **50** 599–605

Vastenhouw B and Beekman F J 2007 Submillimeter total-body murine imaging with USPECT I *J. Nucl. Med.* **48** 487–93

Vastenhouw B, van der Have F, van der Linden A J A, von Oerthel L, Booij J, Burbach J P, Smidt M P and Beekman F J 2007 Movies of dopamine transporter occupancy with ultra-high resolution focusing pinhole SPECT *Mol. Psychiatry* **12** 984–7

Verhoeff N P L G 2004 Ligands for neuroreceptor imaging by positron or single-photon emission computed tomography *Nuclear Medicine in Clinical Diagnosis and Treatment* 3rd edn, ed P J Ell and S S Gambhir pp 1275–94

Warwick J M 2004 Imaging of brain function using SPECT *Metab. Brain Dis.* **19** 113–23

Zito F, Savi A and Fazio F 1993 CERASPECT: a brain-dedicated SPECT system-performance evaluation and comparison with the rotating gamma camera *Phys. Med. Biol.* **38** 1433–42